Prospects of a superradiant laser based on a thermal or guided beam of ^{88}Sr

Mikkel Tang [1,2] Stefan A. Schäffer [2] and Jörg H. Müller [1]

[1]*Niels Bohr Institute, University of Copenhagen, Blegdamsvej 17, 2100 Copenhagen, Denmark*
[2]*Van der Waals-Zeeman Institute, Institute of Physics, University of Amsterdam, Science Park 904, 1098 XH Amsterdam, Netherlands*

The prospects of superradiant lasing on the 7.5-kHz-wide $^{1}S_0$ - $^{3}P_1$ transition in ^{88}Sr is explored by using numerical simulations of two systems based on realistic experimental numbers. One system uses the idea of demonstrating continuous superradiance in a simple, hot atom beam with high flux, and the other system is based on using ultracold atoms in a dipole guide. For the hot-beam system we consider a range of atom beam parameters as well as the impact of a scheme to discard fast atoms along the cavity axis. We find that the system achieves lasing above a flux of 2.5×10^{12} atoms/s and that it is capable of outputting hundreds of nanowatts and suppressing cavity noise by a factor of 20–30. The relativistic transverse Doppler shifts cause a shift in the lasing frequency on the order of 500 Hz. For the cold-atom beam we account for decoherence and thermal effects when using a repumping scheme for atoms confined in a dipole guide. This is done by treating recoils and state-dependent forces acting on atoms in the dipole guide within the framework of the stochastic master equation. We find that the output power is on the order of hundreds of picowatts; however, transverse Doppler shifts can be neglected, and cavity noise can be suppressed on the order of a factor of 50–100. Additionally, we show that both systems exhibit local insensitivity to fluctuations in atomic flux.

I. INTRODUCTION

The precision of state-of-the-art frequency references based on optical cavities [1–3] is limited by thermal fluctuations in the mirrors [4]. This has motivated the development of frequency references based on superradiant lasers with reduced sensitivity to cavity noise [5]. These operate using atomic transitions which are much narrower than the cavity linewidth, so that the spectral properties of the atoms dominate over the resonator. Alkaline-earth atoms such as strontium are a promising source due to a level structure allowing for efficient laser cooling and the availability of narrow, forbidden transitions. So far pulsed [6–13] and quasicontinuous superradiant lasing [9,14] has been investigated extensively, both experimentally and theoretically. Achieving continuous superradiant lasing experimentally is an ongoing challenge, but theoretical studies have considered continuous superradiance both in ultracold-atom systems [5,15–26] and in hot-atom systems [27–31] that may be simpler to realize with higher possible atom fluxes. Some studies have also specifically investigated the impact of inhomogeneous broadening effects [32,33]. The push towards precision measurement applications, including continuous superradiance, has also sparked development in sources of atomic beams [34–38] which can meet the technical requirements for lasing on very narrow transitions.

Here we investigate the prospects of continuous superradiant lasing on the $^{1}S_0$ - $^{3}P_1$ intercombination line in ^{88}Sr. We aim to capture all the vital physical effects present in a realistic physical system [35,39] and to bridge the gap to more idealized theoretical descriptions which often omit, e.g., details about phase-space distributions, thermal effects, optical forces, and realistic energy-level schemes for the sake of simplicity and computational advantages. We consider a cold-atom system based on the source in [35], and a hot-atom system [39] based on a recent theoretical proposal [27]. We use numerical simulations to investigate these two systems, the requirements to overcome the lasing threshold, and the influence of cavity fluctuations. In Sec. II we present a simple cooperativity model for the cold-atom system which highlights the parameter regime that is necessary to obtain lasing. In Sec. III we introduce the full theoretical model used to study superradiant lasing quantitatively in the cold- and hot-atom systems. In Secs. IV and V we present the expected lasing dynamics and relevant physical effects for the cold- and hot-beam systems, respectively.

II. SYSTEM AND COOPERATIVITY MODEL

The systems we describe here consist of ^{88}Sr atoms propagating through a cavity while initially in the excited $^{3}P_1$ state. In this section we will consider the cold-atom system. To achieve superradiant lasing the atoms must preferentially emit into the cavity mode, and this process competes with emission into the environment and decoherence. In terms of the collective cooperativity we can write this condition as

$$C_0 N \gamma \gg \Gamma_{\text{decoh}}, \tag{1}$$

where C_0 is the single-atom cooperativity, N is the number of atoms, γ is the decay rate of the excited energy level, and Γ_{decoh} is the dephasing rate of the dipole, including, e.g., Doppler broadening and decoherence from pumping. In terms of γ, the cavity linewidth κ, and the atom-cavity coupling g, we have $C_0 = 4g^2/\gamma\kappa$. In a realistic scenario the cavity mode is a standing wave and has a Gaussian intensity distribution, giving a spatial dependence $g(r, z)$. We approximate the atomic-beam density profile by a Gaussian in the plane perpendicular to its propagation axis, characterized by the standard deviation σ_y in the dimension that is also perpendicular to the cavity axis, leading to an overlap integral with the cavity mode. Thus, if we have a beam of excited Sr atoms propagating at a speed v, we can rewrite the lasing condition in terms of experimental parameters as

$$\frac{6\sqrt{2\pi}c^3}{\omega^2}\frac{\Phi}{LW\kappa v}\sqrt{\frac{\frac{W}{\sigma_y}}{\left(\frac{W^2}{\sigma_y^2}\right)^2 + 4}}\frac{\gamma}{\Gamma_{decoh}} \gg 1. \qquad (2)$$

The first fraction is constant for a given transition frequency ω. In the second fraction we see that the cooperativity increases linearly with the flux Φ and decreases if we increase the mode volume (cavity length L or waist radius W), the loss rate κ, or propagation velocity v, which affects the density for a fixed flux. The term under the square root is a scaling between 0 and 1 related to the overlap of the atomic beam with the cavity: If the cavity waist is much larger than the atomic beam, it yields 1, but if it is much smaller than the beam, it approaches 0. The final term, γ/Γ_{decoh}, can approach 1/2 (for the lowest possible decoherence rate), but given a finite temperature T and a repumping rate from the ground state w, the term will generally be smaller. If the lasing condition is fulfilled and the atom-cavity overlap is good, the output power from the cavity can approach the limit set by energy conservation of $P_{max} = \hbar\omega\Phi$. If repumping is included at the rate w and we assume only atoms within the cavity waist participate in lasing, this limit increases to approximately $P_{max} = \hbar\omega\Phi(1 + 2wW/v)$.

Using a dipole guide enables confinement of atoms down to tens of micrometers, combined with propagation velocities on the order of 10 cm/s and microkelvin temperatures. High atomic flux in such a system was shown to be possible in [35]. Although we consider the cold-atom system for now, we also note the most significant qualitative differences of the hot-beam system: In this system the thermal decoherence rate and much higher propagation velocities lead to a much higher flux requirement to achieve lasing. Additionally, the output power when lasing cannot exceed $\hbar\omega\Phi$ due to the lack of repumping. However, this value is still orders of magnitude higher than P_{max} for the cold-beam system due to the much higher flux.

III. THEORETICAL MODEL

In this section we will describe the general and common features of the numerical models applied to the cold- and hot-beam systems for quantitative evaluations, illustrated in Fig. 1. The framework described here was previously applied in [10,11], where it was compared to experiments and used to describe pulsed lasing dynamics in the millikelvin tem-
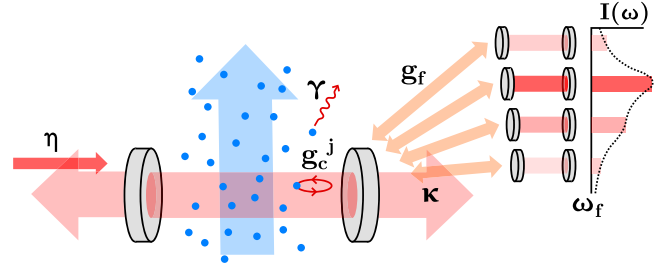

FIG. 1. Illustration of a superradiant laser composed of atoms traversing an optical cavity. Each atom couples to the cavity mode at a rate g_c^j. Dissipation into the environment occurs at the spontaneous emission rate γ for atoms and the total photon loss rate κ of the cavity. In the model, a driving laser with rate η is used to initiate the atom-cavity interaction, and the power spectrum of the laser $I(\omega)$ can be extracted via an array of filter cavities weakly coupled to the main cavity at rates g_f.

perature regime. At the core, the cold- and hot-beam models are based on a Tavis-Cummings Hamiltonian, including a driving laser term for initiating the superradiant dynamics, and an array of filter cavities [11,19] for extracting spectral information:

$$H = \hbar\omega_c a^\dagger a + \sum_{j=1}^{N} \hbar\omega_e^j \sigma_{ee}^j + \sum_{k=1}^{N_f} \hbar\omega_f^k f_k^\dagger f_k$$

$$+ \frac{1}{2}\hbar\eta(ae^{-i\omega_d t} + a^\dagger e^{i\omega_d t})$$

$$+ \sum_{j=1}^{N} \hbar g_c^j(\mathbf{r_j})(\sigma_{ge}^j + \sigma_{eg}^j)(a + a^\dagger)$$

$$+ \sum_{k=1}^{N_f} \hbar g_f(a + a^\dagger)(f_k + f_k^\dagger). \qquad (3)$$

Here ω_i are the resonance frequencies of the cavity ($i = c$), the jth individual atom ($i = e$), driving laser ($i = d$), or kth filter cavity ($i = f$); a (f_k) is the (kth filter) cavity-field annihilation operator, and σ_{xy}^j is the spin operator of the jth atom. N is the number of atoms in the simulation, and N_f is the number of filter cavities chosen to obtain a given spectral resolution. η is the driving rate of a laser that is used to initiate the lasing dynamics at the start of a simulation, which is subsequently set to zero. The filter cavities in the Hamiltonian are coupled to the main cavity with a tiny constant g_f, such that physical back-action on the main cavity can be neglected. The jth atom couples to the cavity at a rate $g_c^j(\mathbf{r_j})$ which depends on its position at a given time. In terms of system parameters, with the cavity aligned along the z axis, it is given by

$$g_c^j(\mathbf{r_j}) = \sqrt{\frac{6c^3\gamma}{W^2 L\omega_E^2}} \sin\left(\frac{\omega_c}{c}z_j\right)\exp\left(\frac{x_j^2 + y_j^2}{W^2}\right), \qquad (4)$$

where ω_E refers to the unperturbed frequency of the lasing transition for an atom at rest. C_0 is defined by the maximum coupling rate g_c^{max}, given by the square-root term. The classical Doppler effect in the atom-cavity interaction arises from

the variations in g_c^j over time for moving atoms. The motion of each individual atom is treated classically.

The Hamiltonian is used to derive a set of differential equations for the atom and cavity states in first-order mean-field theory, which are numerically integrated over time. In addition to the Hamiltonian dynamics, atoms also couple to the environment at the spontaneous emission rate γ, and photons from the cavity leak at a total rate κ. This relates to the total output power by $P_{\text{out}} = \hbar\omega_c \kappa n$, where n is the cavity photon number. These dissipative dynamics are described via Lindblad superoperators for the hot-beam model or similar terms in the stochastic master equation for the cold beam. The cold-beam system additionally involves more levels and pumping terms due to the repumping scheme.

In contrast to previous applications of the model, we here describe a system where atoms continually enter and exit a cavity. Thus, the number of atoms continually fluctuates: Based on the atom flux a number of new atoms are periodically introduced, and existing atoms are deleted if they move significantly out of the cavity mode. Furthermore, we here assume atoms are pumped incoherently, and we therefore include a classical driving laser to initiate the lasing dynamics—in a real system this occurs due to quantum fluctuations, which are not included in first-order mean-field theory. This drive is turned off when we evaluate the steady-state parameters. In this numerical approach the power spectrum of the superradiant laser can be determined from the relative populations of filter-cavity photons or, alternatively, from the amplitude spectrum from Fourier transforming $\langle a(t)\rangle$ (in only first-order mean-field theory). Therefore, the Fourier limit also determines the simulation time required to resolve a given feature or linewidth.

IV. LASING FROM A GUIDED COLD BEAM

A flux of up to $\Phi = 3 \times 10^7$ atoms/s with a mean propagation velocity of 0.084 m/s has been demonstrated in a guided beam of cold ^{88}Sr [35], but later improvements to the experimental system showed that up to $\Phi = 3 \times 10^8$ atoms/s is realistic [40]. However, the 21-µs decay time of $^3P_1$ renders it impractical to simply excite such a slow atom beam before entering a cavity several tens of microns across. Even if modifications could be made to maintain inversion during passage of a cavity, the atom flux limits the output power to the order of tens of picowatts at most. Therefore, we find that the most interesting regime for superradiant lasing based on this system is realized by continuously repumping the atoms within the cavity. A repumping scheme which has been used to study quasicontinuous superradiant lasing in a magneto-optically trapped ensemble was demonstrated in [9]. Since many photon recoils are imparted during each repumping cycle, the atoms can heat up significantly using this scheme. This makes it necessary to shelve the atoms in long-lived states until their position within the Gaussian mode provides a sufficiently high coupling rate for them to emit primarily into the cavity rather than the environment. Based on this, we consider the system depicted in Fig. 2. Here the atoms start in the long-lived state $^3P_0$ and propagate along the x axis through the cavity. Within the cavity they are continuously repumped by lasers pointing along the y axis. To describe this system the
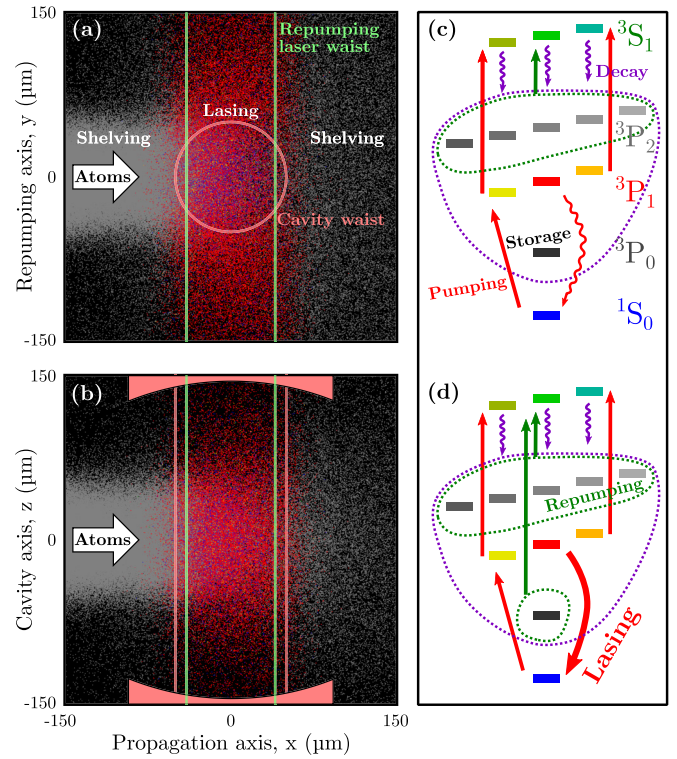

FIG. 2. Illustration of the cold-beam system, viewed along (a) the cavity axis and (b) the repumping axis. Each atom is color-coded by its state according to (c) and (d) (without the variations in gray), where the shelving-and-pumping scheme is illustrated. The atoms are initially shelved in $^3P_0$. Within the cavity they are pumped to $^3P_1$ $m_J = 0$ and contribute to lasing, heat up, and disperse due to repumping, primarily along the repumping axis. (c) Pumping scheme to store atoms in $^3P_0$ before entering the cavity. (d) Pumping scheme to transfer atoms to $^3P_1$ $m_J = 0$ for the lasing process.

two-level model is extended to include $^3P_0$ and the Zeeman sublevels of $^3P_1$, $^3P_2$, and $^3S_1$, yielding the set of equations for the evolution of atom and cavity states given in Appendix A. The initial atom velocities are based on radial temperatures of 890 nK and 29 µK along the propagation axis [35], and the distribution in the propagation direction is also treated as Gaussian, with a mean velocity of 0.084 m/s. We include the forces of a dipole guide on the atoms, with a wavelength of 913.9 nm, waist radius of 165 µm, and power of 15 W. These forces are calculated on each atom depending on their position and internal state at a given time. Repumping can change the velocity of the initially cold atoms significantly: An average of 15 photon recoils are imparted to bring an atom from $^1S_0$ to $^3P_1$ $m_J = 0$ (8 from repumping lasers and 7 from decays). The recoils are modeled by using a conditional stochastic master equation (SME) to treat spontaneous decays and the majority of the pumping laser interactions. In this way the model can account for heating of the atoms both due to the recoils and also due to the abrupt changes in state in the dipole guide potential. To minimize heating along the cavity axis we choose the repumping lasers to be orthogonal to the cavity axis. Collisions between atoms are not taken into account.

Two of the pumping laser interactions, from $^1S_0$ to $^3P_1$ $m_J = -1$ (689 nm) and from $^3P_1$ $m_J = -1$ to
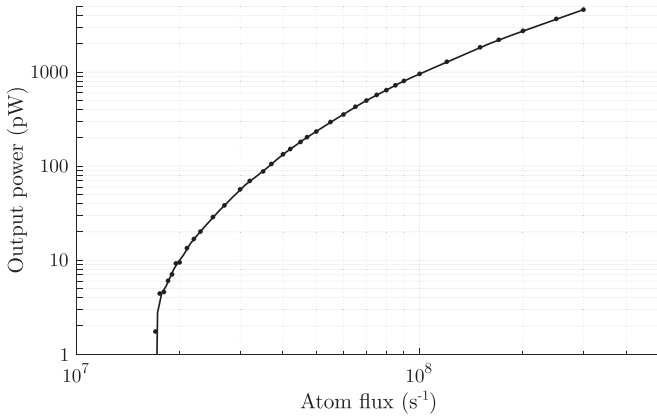
FIG. 3. The cavity output-power dependence on atom flux Φ. A flux of 10^8 s^{-1} yields 4.6×10^4 atoms in the cavity waist at steady state. The line shows a moving mean with a span of two points.

FIG. 4. The shift in lasing frequency Δ_L for varying atom flux at three different cavity detunings Δ_{cE}. The local cavity-pulling coefficient can be determined by the distance between the curves. Experimental parameters can be chosen to achieve a lasing frequency shift of zero within a range of fluxes, in this case around 8×10^7 s^{-1}. Lines show a moving mean with a span of two points.

$^3S_1$ $m_J = -1$ (688 nm), are treated using coherent interactions, using the SME quantum jumps only for dissipation. Thus, light shifts are included in the model, which can result in shifts in the superradiant lasing frequency. Light shifts on the lasing transition from the 679- and 707-nm repumping lasers can be made negligible (<1 Hz) by choosing a suitable "magic" intensity ratio. We assume a magnetic field of 0.476 G pointing along the x axis, giving a 1-MHz splitting of the $^3P_1$ Zeeman levels. Thus, the dipole guide beam, polarized along the y axis, is magic for the lasing transition. The 688-nm repumping laser is linearly polarized along the x axis, driving the π transitions from $^3P_1$ (except $m_J = 0$ because that is forbidden), while the 689-, 679-, and 707-nm lasers are polarized along the z axis, driving $\sigma_\pm$ transitions. Since the 688-nm laser has to drive atoms from both $m_J = -1$ and $+1$ to the corresponding $^3S_1$ levels, it is chosen to be equally detuned from both transitions (333 kHz). The other repumping lasers are equivalently tuned symmetrically, except the 689-nm repumper, which is tuned to resonance with the Zeeman-shifted transition of $^1S_0$ - $^3P_1$ $m_J = -1$. Its effect on the $m_J = +1$ transition is neglected due to the large detuning.

The performance of the system can be evaluated in terms of the cavity-pulling coefficient $c_{\text{pull}} = \Delta_L / \Delta_{cE}$, which depends on the shift in lasing frequency Δ_L for a given cavity detuning Δ_{cE}. If $c_{\text{pull}} = 1$, the cavity fully determines the lasing frequency, and if it is zero, the lasing frequency is determined fully by the atom transition, and the laser is maximally insensitive to cavity-length fluctuations. In addition the output power is an important parameter since a power in the picowatt regime can be demanding to detect and use as a frequency reference. A third parameter that is experimentally important is the cavity length. A short cavity length gives a stronger atom-cavity coupling, which means the finesse can be lowered to achieve the same lasing threshold, enabling one to operate further in the bad cavity regime. However, a short cavity also requires finer control of the piezo voltage to keep fluctuations in the resonance frequency acceptable.

Assuming a cavity length of 25 mm and waist radius of 50 μm, we find that the optimal cavity linewidth will be on the order of tens of megahertz, and here we choose 20 MHz to obtain a lasing threshold below 2×10^7 atoms/s. The expected output power for a given flux is shown in Fig. 3. Here the 679-
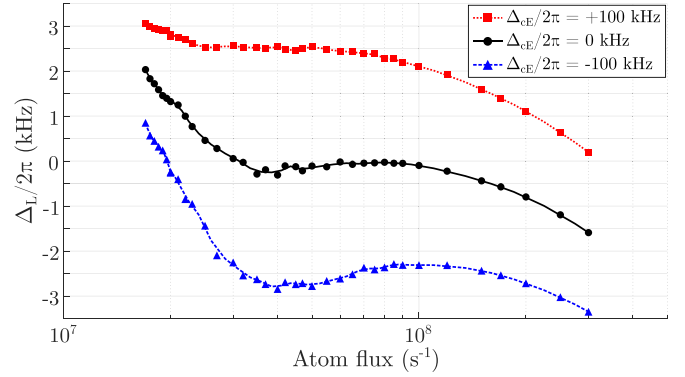
and 707-nm repumping lasers have waist radii of 40 μm along the propagation axis. The 689- and 688-nm pumping lasers have uniform beam profiles, with Rabi frequencies $\chi/2\pi$ of 100 kHz and 1 MHz, respectively.

The lasing frequency obtained in simulations is depicted in Fig. 4 for varying atom flux at three different cavity detunings. Ideally, the superradiant lasing frequency should have no offset from the atomic transition (corresponding to the middle curve in Fig. 4 staying at zero). However, we do see offsets which are attributed to light shifts from the pumping lasers. Generally, the flux dependence is nontrivial as the atomic inversion, and thus light shift, depends on the flux. But for a certain choice of repumping rates, the frequency offset is zero within a range of atom fluxes, as seen near 8×10^7 s^{-1} in Fig. 4. Here the lasing frequency shift is also locally independent of the atom flux for small detunings, which removes the sensitivity to noise and slow variations in the flux from the atom source. We find that this local immunity to atom-flux fluctuations also depends on a wide number of parameters, such as the sizes of the repumping beams. For smaller repumping regions, the curves in Fig. 4 become more linear, such that there is no flux-immune plateau when using waists of 30 μm. We attribute these flux-immune properties partially to the flux dependence of the heating rate from repumping. When the pumping region is smaller, the atoms are heated for a shorter duration, leading to a more monotonic curve for the frequency shifts. Thus, the curves can be engineered by variation of experimental parameters.

In Fig. 4 the cavity-pulling coefficient can be determined from the relative distance between the curves at different cavity detunings and varies from 0.01 to 0.025. Near the lasing threshold, the atoms do not emit many photons; thus, they experience only a few repumping cycles and relatively low heating rates. This results in an average temperature within the cavity waist, along the cavity axis, of $T_z = 34$ μK for $\Phi = 2 \times 10^7$. As the atom flux increases, the steady-state cavity photon number and thus the atomic emission rate $g\sqrt{n}$ increase, leading to more repumping cycles and higher temperatures. The highest cavity-pulling coefficients are obtained for a flux near 5×10^7 s^{-1}, where $T_z = 54$ μK. For even higher

flux the cavity pulling starts to decrease again, as the effect of the high number of atoms starts to become more significant than the effects from heating for a flux of 3×10^8 s^{-1}, with $T_z = 76$ μK.

Since thermal effects increase cavity pulling in the system, we additionally investigated the effect of an intracavity optical lattice at the magic wavelength of 913.9 nm. Such a lattice could potentially prevent atoms from propagating along the cavity axis significantly. We find that the lattice begins to have a significant impact when the power is in the range of 1–10 W. However, we find that the lattice generally increases cavity pulling due to the repumping scheme in combination with the steep optical potentials of the lattice. The fact that the optical potential depth varies for different states leads to significant additional heating, which is revealed by the quantum jumps of the SME.

The Purcell rate, $\gamma_P = C_0 \gamma = 4(g_c^{max})^2/\kappa$, of $2\pi \times 82$ Hz offers a simple estimate of the linewidth [5], but further narrowing can occur within the superradiant lasing regime [19], in which the cold-beam system operates. The simulations include a number of effects which may also limit the linewidth—the thermal effects and discrete spontaneous emission events from $^3P_1$ into the environment. On the other hand, they neglect spontaneous emission into the cavity mode. The linewidth in simulations is Fourier limited to 5 Hz after 200 ms, indicating that the effects that are included do not limit the system beyond the theoretical estimate.

The spatial dependence of the dynamics are shown in Fig. 5, evaluated for $\Phi = 10^8$ atoms/s. In Fig. 5(a) a breakdown of the atomic states is shown as a function of position in the beam. Due to the Gaussian repumping intensity profiles, the $^3P_1$ population increases gradually towards the center of the repumping beams. There is additionally a small increase in inversion towards the exit side of the cavity, as the atom beam heats up and interacts less efficiently with the cavity mode. In Fig. 5(b) the average number of emission events from $^3P_1$ into the cavity (red line) or environment (dashed purple line) is shown as a function of position. For this flux and repumping rate, we see each atom can emit upwards of 40 photons into the cavity and 25 into the environment before escaping. This demands on the order of 1000 photon recoils during the repumping process, highlighting the importance of this heating mechanism. Note that atoms escaping near $x = 300$ μm are generally the fastest and will thus not emit as many photons as those that spend a long time inside the cavity waist, emit many photons, but eventually heat up and escape along the repumping axis. A few atoms also escape from the direction they originally came from and contribute to the nonzero average value for $x < 100$ μm. In Fig. 5(c) we show the spatially dependent temperature profile in each dimension. The fact that the atoms are repumped and change state in the guided beam results in nonadiabatic dynamics because the potential depth is different for each state. Photon recoils from the repumping process heat the atoms mainly along the y axis but also to a smaller degree along the x and z axes due to the spontaneously emitted photons.

As the heating mechanism arising from the combination of the optical dipole guide potential with repumping limits the performance of this cold-beam system, the idea of additionally cooling the atoms on transitions encountered within a repump-
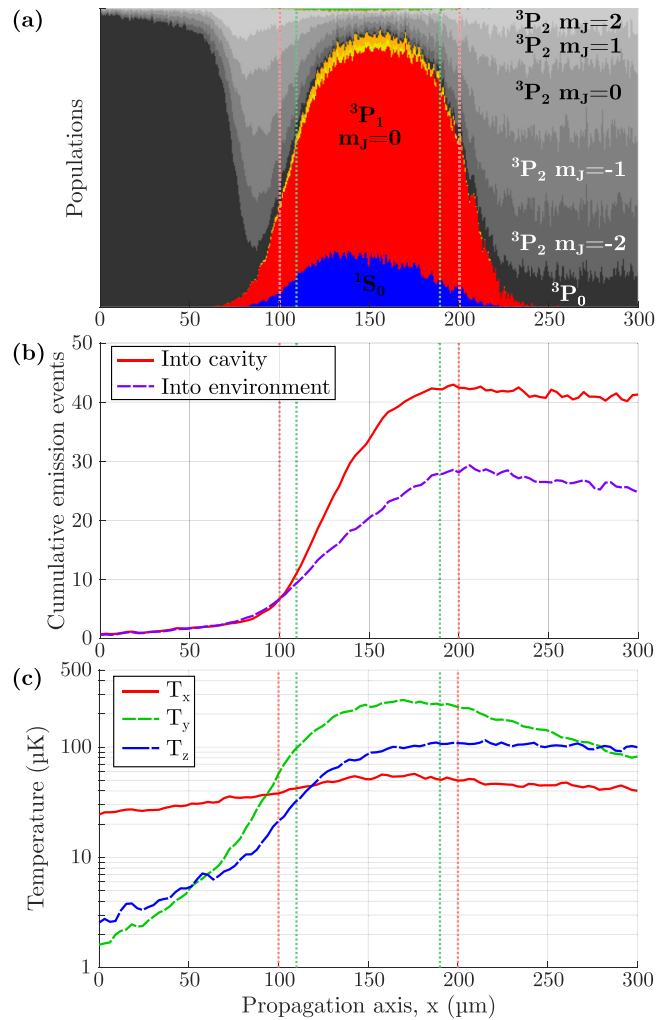

FIG. 5. Spatial profile of an actively lasing cold-atom beam for a flux of $\Phi = 10^8$ atoms/s. (a) Histogram of the spatial distribution of states (yellow shows $^3P_1$ $m_J = -1$, orange shows $^3P_1$ $m_J = 1$, green shows $^3S_1$, and other colors are as indicated in the panel). Atoms start in $^1P_0$. Once they reach the cavity (waist: red dotted lines), repumping lasers at 679 and 707 nm (waist: green dotted lines) enable inversion on the lasing transition. (b) The mean accumulated number of emission events in the steady-state regime of an atom as a function of its x position, throughout its trajectory up to that point. Note some atoms escape on the left and along the repumping axis near $x = 150$ μm after interacting with the cavity mode and pumping lasers, while faster atoms tend to interact less and escape on the right. In this regime on the order of 40 photons can be emitted from each atom into the cavity before exiting. (c) Temperature profile along each dimension (T_x: propagation axis, T_y: repumping axis, T_z: cavity axis) as a function of position. The temperature profile is a result of interactions with the repumping lasers and optical dipole guide.

ing cycle [5] could potentially improve the performance of the system. If the cooling is efficient enough to keep atoms well confined within a lattice along the cavity axis, simulations suggest cavity pulling might be improved by an order of magnitude. Alternatively, a different pumping scheme and dipole guide wavelength may be used to reduce the heating rate. This could be done by reducing the number of recoils per repumping cycle or reducing the variations in
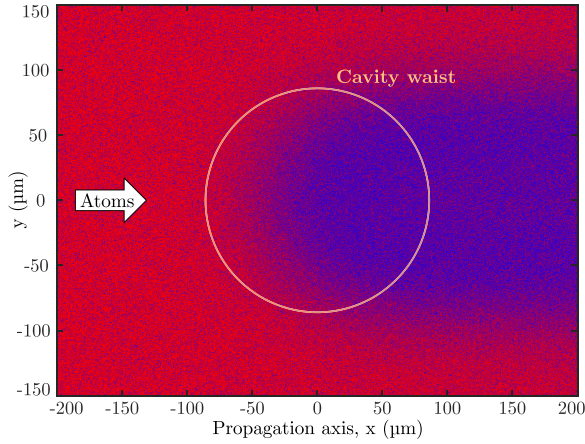
FIG. 6. Illustration of the hot-beam system. Atoms are color-coded according to their state ($^1S_0$ in blue and $^3P_1$ in red). Due to velocity selection in this simulation, some of the atoms start in $^1S_0$. As the atoms pass through the cavity (waist marked by circle), they will tend to emit a photon and change state to $^1S_0$.

polarizability during a pumping cycle by utilizing different transitions and/or a different magic wavelength for the dipole guide.

V. LASING FROM A HOT-ATOM BEAM

A promising and technically simpler source for superradiant lasing is a thermal beam of strontium atoms emanating directly from an oven, cooled transversely on the $^1S_0$ - $^1P_1$ transition to bring the radial temperature to the millikelvin regime [34,36,37]. This concept was explored theoretically in [27,29–31]. Here we investigate this proposal with the physical constraints of a real system operating on the $^1S_0$ - $^3P_1$ transition of ^{88}Sr, as illustrated in Fig. 6. We assume the atoms can start in the excited state $^3P_1$ or ground state $^1S_0$ and the atoms are treated as a two-level system. Due to the high number of atoms we use a clustering approach to simulate the hot-beam system, treating atoms in groups of 100 where each atom in a group has the same position, velocity, and internal state. This approximation does not systematically influence the power and frequencies presented here but does artificially inflate dynamic cavity-field phase and power fluctuations by a factor of $\sqrt{100}$. The atom velocities are drawn from Gaussian distributions based on a temperature of 3.6 mK orthogonally to the propagation axis and from a thermal beam distribution in the propagation direction with a most probable velocity of 400 or 450 m/s. At these velocities the relativistic transverse Doppler shift becomes significant and is therefore included in the transition frequency of each atom ω_e^j, which is typically on the order of -500 Hz. Equations describing the hot-beam system are given in Appendix B.

We can expect that the cavity pulling can be reduced by preventing atoms from moving along the cavity axis. The effect of this motion was studied for the fast beam, where a bistable regime was found when atoms collectively moved across half a wavelength during transit [31]. Thus, to reduce the influence of atoms that move farther than half a wavelength while traversing the cavity waist, we include a velocity-selection stage [34] in our simulations. In this scheme
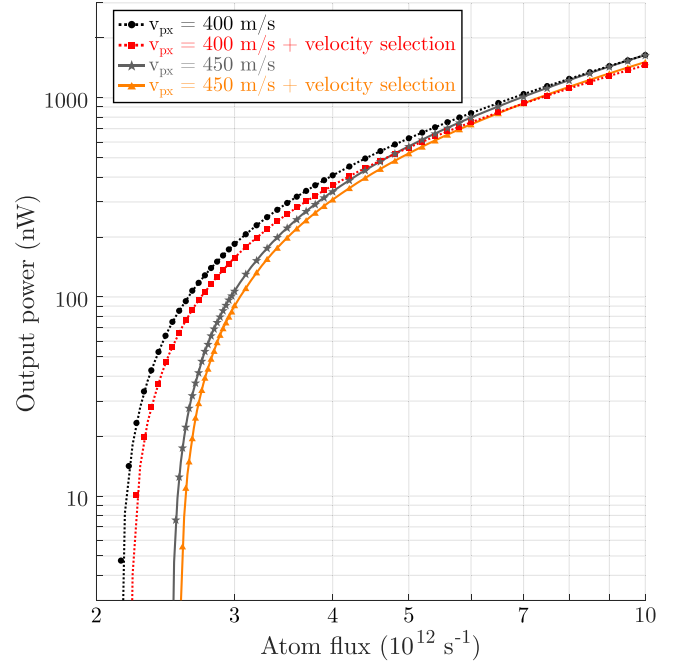

FIG. 7. Expected cavity output power as a function of atom flux through the cavity-mode waist for two values of the most probable atomic velocity, with and without the velocity-selection scheme. A flux of 10^{13} s^{-1} corresponds to $\{3.71, 3.28\} \times 10^6$ atoms in the cavity waist for $v_{px} = \{400, 450\}$ m/s. The velocity-selection scheme leads to a decrease in output power and a slight increase in lasing threshold. Lines show a moving mean.

the atoms are initially shelved in a long-lived state according to the criterium $|v_z| < \lambda \times v_{px}/4W$, where v_z is the velocity along the cavity axis, v_{px} is the most probable velocity in the propagation direction, and W is the cavity waist radius. The atoms that move too quickly along the cavity axis thus remain in $^1S_0$. These atoms are subsequently shifted in momentum space using a resonant laser on the $^1S_0$ - $^1P_1$ transition such that they do not interact with the cavity photons. This requires a Doppler shift significantly greater than the power broadening of the lasing transition due to the intracavity field, for which a push by a few meters per second is sufficient in the considered regime. Since this is done by a laser along the cavity (z) axis, the selection is imperfect, as some atoms may move slow enough along z to not be selected but sufficiently slow along x that they still cross half a wavelength.

Since multiple stages of loading atoms into magneto-optical traps and guided beams are not necessary, a much higher atomic flux can be obtained through the cavity than in the cold-beam system; thus, expected values are on the order of 10^{12}–10^{13} atoms/s [34]. For this system, with a cavity length of 27.36 mm, linewidth of $2\pi \times 53.9$ MHz, and waist radius $W = 86$ μm, we find the lasing threshold is reached between 8 and 8.5×10^5 atoms within the cavity waist. This atom number is reached for different atom fluxes depending on the mean propagation velocity (see Fig. 7). The threshold flux is on the order of $\Phi = 2.5 \times 10^{12}$ atoms/s, and an output power on the order of 1.5 μW can be achieved at 10^{13} atoms/s.

Due to the transverse Doppler shifts, cavity pulling will occur relative to a frequency that is shifted depending on
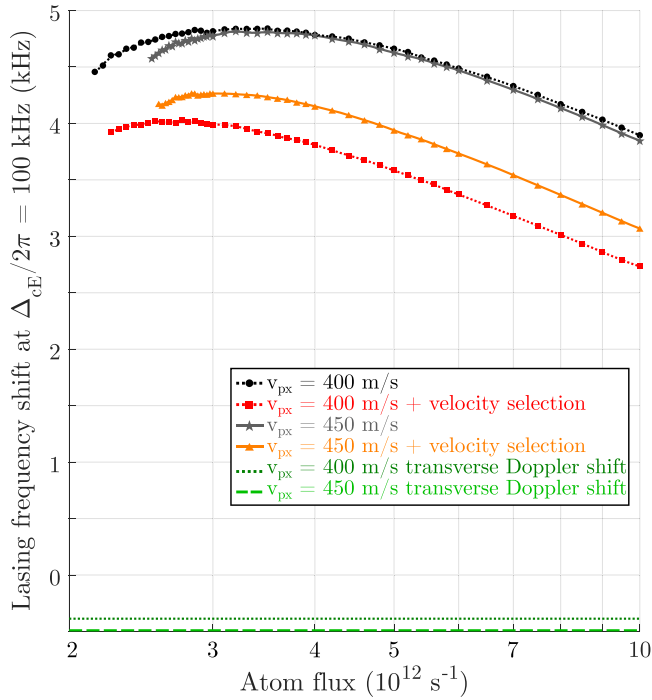
FIG. 8. Lasing frequency shift as a function of atomic flux compared for the two most probable atomic velocities. The expected frequency shift is shown with and without the velocity-selection scheme for a fixed cavity detuning of 100 kHz. The significant transverse Doppler shift in the ensemble lasing frequency is illustrated for the two velocities. The cavity-pulling coefficients are below 0.06, and we find the velocity-selection scheme reduces cavity pulling 10%–25% in this regime. Lines show a moving mean.

the transverse Doppler shifts of the atoms in the ensemble. As the atoms interact differently depending on their velocity and this interaction also depends on the atom flux, the exact resonance frequency of the ensemble is nontrivial, but it will be close to the transverse Doppler shift at v_{px}. We redefine the pulling coefficient in the presence of transversely shifted atomic resonance frequencies to $c_{\text{pull}} = (\Delta_L - \Delta_D)/(\Delta_{cE} - \Delta_D) \approx (\Delta_L - \Delta_D)/\Delta_{cE}$, where Δ_D is the shift in the atom ensemble resonance caused by transverse Doppler shifts. The approximation holds for $\Delta_{cE} \gg \Delta_D$. The cavity-pulling characteristics are shown in Fig. 8 for a fixed cavity detuning of $2\pi \times 100$ kHz. Here we find cavity-pulling coefficients in the range of about 0.03 to 0.06, which are locally independent of the atom flux slightly above threshold. These pulling coefficients represent the behavior for small detunings, but in general the pulling coefficients also vary for changes in detuning that are on the order of the cavity linewidth. We also see that the velocity-selection scheme reduces cavity pulling on the order of 15%, although in a system where the cutoff velocity is considered a free parameter one could reduce this further at higher flux values to reduce cavity pulling further, at the cost of a lower output power. In the simulations with $v_{px} = 450$ m/s the velocity-selection scheme has a smaller impact, as more atoms follow the selection criterium.

For the hot-beam system considered here, the Purcell rate is $2\pi \times 9.4$ Hz. As for the cold-beam system, the simulations neglect spontaneous emission into the cavity mode but do not indicate a broadening of the linewidth from other sources. Our simulations of the system are well within the steady-state superradiant phase reported in [29] characterized by one spectral peak but transitions to the reported chaotic and multicomponent superradiant phases for temperatures above $T_z \sim 15$ mK in the absence of velocity selection.

VI. CONCLUSION

We found that the hot-beam approach can realistically produce an output power of hundreds of nanowatts to microwatts on the $^1S_0$ - $^3P_1$ transition in ^{88}Sr, and the hot-beam system investigated here is capable of suppressing cavity noise by a factor of 20–30. Implementation of a velocity selection scheme can contribute about 10%–25% to this suppression factor. The exact lasing frequency is shifted by approximately 500 Hz due to transverse Doppler shifts. On the other hand, this effect is negligible in the cold-atom system. This system is significantly more complex and relies on repumping of atoms within the optical cavity. To consider this in detail we have accounted for all the atomic states involved in repumping within the framework of the stochastic master equation. This has enabled us to treat the variations in optical potentials experienced by the atoms during repumping and its effect on temperature in addition to photon recoils. We have found these effects have a large impact on the lasing dynamics, causing a reduction in power and increased sensitivity to cavity noise compared to what may be expected from simpler models. Therefore, such effects may also be relevant to consider in other concrete superradiant lasing schemes relying on repumping, as they are typically omitted in simplified theoretical models. Our simulations indicated the cold-beam system can provide a power on the order of hundreds of picowatts and suppress cavity noise by a factor of 50–100. It furthermore has a number of experimental parameters which can be optimized to minimize the sensitivity of the lasing frequency to fluctuations in the atom flux. Both approaches using the $^3P_1$ state in Sr to generate superradiant lasing are promising as reference laser candidates that can provide output power levels high enough to be easily detectable, which is advantageous compared to much narrower clock lines.

APPENDIX A: COLD-BEAM MODEL EQUATIONS

For the cold-beam system, 13 atomic states are involved in lasing and repumping, which will be referred to by the subscripts:

$$g = {}^1S_0, n = {}^3P_0,$$
$$(i, e, u) = {}^3P_1 \, m_J = (-1, 0, 1),$$
$$(x, y, z) = {}^3S_1 \, m_J = (-1, 0, 1),$$
$$(p, q, r, s, t) = {}^3P_2 \, m_J = (-2, -1, 0, 1, 2).$$

The total Hamiltonian of the cold-beam system is given by Eq. (3) plus the following additional terms for the pumping interactions which are treated coherently, with Rabi frequencies χ_{li}^j from $|g\rangle$ to $|i\rangle$ and χ_{lx}^j from $|i\rangle$ to $|x\rangle$:

$$
\begin{aligned}
H = &\sum_{j=1}^N \hbar \omega_i^j \sigma_{ii}^j + \hbar \omega_x^j \sigma_{xx}^j \\
&+ \sum_{j=1}^N \hbar \frac{\chi_{li}^j}{2} \left(\sigma_{gi}^j + \sigma_{ig}^j \right) \left(e^{ik_{li}r_j - i\omega_{li}t} + \text{c.c.} \right) \\
&+ \sum_{j=1}^N \hbar \frac{\chi_{lx}^j}{2} \left(\sigma_{ix}^j + \sigma_{xi}^j \right) \left(e^{ik_{lx}r_j - i\omega_{lx}t} + \text{c.c.} \right).
\end{aligned} \quad \text{(A1)}
$$

Here, for example, $k_{li}r_j$ denotes the dot product of the laser wave vector with the atomic position vector, and ω_{li} denotes the laser frequency. Within first-order mean-field theory the expectation value of the cavity photon number is $\langle n \rangle \approx \langle a \rangle^* \langle a \rangle$, where the expectation value of the lowering operator evolves according to (from now on dropping angle brackets for expectation values)

$$
\dot{a} = -\left(i\Delta_{cE} + \frac{\kappa}{2} \right) a - i\frac{\eta}{2} e^{i\Delta_{dE}t} - i\sum_{j=1}^N g_c^j \sigma_{ge}^j. \quad \text{(A2)}
$$

The detuning with respect to the unperturbed atomic transition frequency (chosen as the rotating reference frame) is $\Delta_{cE} = \omega_c - \omega_E$, the cavity linewidth is κ, driving laser frequency is ω_d, and intensity parameter is η. The equation for $\dot{a}$ couples to the atomic coherences on the lasing transition. These are modeled in the framework of the SME, where we will continue to use the σ operator notation but note that they represent stochastic values, e.g., $\langle \rho_{eg}^j \rangle = \langle \sigma_{ge}^j \rangle$. In this framework σ_{ge}^j does not continually decay, and instead, σ_{ee}^j and σ_{ge}^j have a probability within a time interval, $p_j(dt) = \sigma_{ee}^j \gamma_{ge} dt$, to make a quantum jump, collapsing to $\sigma_{gg}^j = 1$ and resulting in all other populations and coherences being zero. However, in the time intervals where this does not happen, the dynamics evolve according to

$$
\begin{aligned}
\dot{\sigma}_{ge}^j = &-i\Delta_{eE}^j \sigma_{ge}^j + ig_c^j a \left(\sigma_{ee}^j - \sigma_{gg}^j \right) \\
&+ i\frac{\chi_{li}^j}{2} \sigma_{ie}^j e^{-ik_{li}r_j + i\Delta_{lil}t} \\
&+ \sigma_{ge}^j \left[-\gamma_{eg}\left(\frac{1}{2} - \sigma_{ee}^j \right) + \gamma_{eg}\sigma_{ii}^j + \gamma_{xi}\sigma_{xx}^j \right], \quad \text{(A3)}
\end{aligned}
$$

where $\Delta_{eE}^j = \omega_e^j - \omega_E$ and ω_e^j is the shifted atomic transition frequency. As there are no Zeeman shifts or significant light shifts on this transition which are not already contained in the coherent dynamics, $\Delta_{eE}^j = 0$. $\gamma_{eg} = 2\pi \times 7.5$ kHz is the exited-state decay rate, and $\Delta_{lil} = 0$ is the laser detuning from the Zeeman-shifted atomic transition frequency. The last line is a renormalization factor which corrects the coherent dynamics in the SME framework. For each atom these equations for $\dot{\sigma}_{ge}^j$ are eventually coupled to all the equations for the 13 relevant atomic levels, which are internally coupled by the pumping scheme and decay paths. For the states $|g\rangle$, $|e\rangle$, $|i\rangle$, and $|x\rangle$ treated with coherences, we get the five following coherence equations:

$$
\begin{aligned}
\dot{\sigma}_{gi}^j = &ig_c^j \sigma_{ei}^j a + i\frac{\chi_{li}^j}{2}\left(\sigma_{ii}^j - \sigma_{gg}^j \right) e^{-ik_{li}r_j + i\Delta_{lil}t} \\
&- i\frac{\chi_{lx}^j}{2} \sigma_{gx}^j e^{ik_{lx}r_j - i\Delta_{lx}t} \\
&+ \sigma_{gi}^j \left[\gamma_{eg}\sigma_{ee}^j - \gamma_{ig}\left(\frac{1}{2} - \sigma_{ii}^j \right) + \gamma_{xi}\sigma_{xx}^j \right], \quad \text{(A4)}
\end{aligned}
$$

$$
\begin{aligned}
\dot{\sigma}_{ix}^j = &i\frac{\chi_{li}^j}{2} \sigma_{gx}^j e^{ik_{li}r_j - i\Delta_{lil}t} \\
&+ i\frac{\chi_{lx}^j}{2}\left(\sigma_{xx}^j - \sigma_{ii}^j \right) e^{-ik_{lx}r_j + i\Delta_{lx}t} \\
&+ \sigma_{ix}^j \left[\gamma_{eg}\sigma_{ee}^j - \gamma_{ig}\left(\frac{1}{2} - \sigma_{ii}^j \right) - \gamma_{xi}\left(\frac{1}{2} - \sigma_{xx}^j \right) \right], \\
& \quad \text{(A5)}
\end{aligned}
$$

$$
\begin{aligned}
\dot{\sigma}_{gx}^j = &ig_c^j \sigma_{ex}^j a + i\frac{\chi_{li}^j}{2} \sigma_{ix}^j e^{-ik_{li}r_j + i\Delta_{lil}t} \\
&- i\frac{\chi_{lx}^j}{2} \sigma_{gi}^j e^{-ik_{lx}r_j + i\Delta_{lx}t} \\
&+ \sigma_{gx}^j \left[\gamma_{eg}\sigma_{ee}^j + \gamma_{ig}\sigma_{ii}^j - \gamma_{xi}\left(\frac{1}{2} - \sigma_{xx}^j \right) \right], \quad \text{(A6)}
\end{aligned}
$$

$$
\begin{aligned}
\dot{\sigma}_{ei}^j = &i\Delta_{eE}^j \sigma_{ei}^j + ig_c^j \sigma_{gi}^j a^\dagger - i\frac{\chi_{li}^j}{2} \sigma_{eg}^j e^{-ik_{li}r_j + i\Delta_{lil}t} \\
&- i\frac{\chi_{lx}^j}{2} \sigma_{ex}^j e^{ik_{lx}r_j - i\Delta_{lx}t} \\
&+ \sigma_{ei}^j \left[-\gamma_{eg}\left(\frac{1}{2} - \sigma_{ee}^j \right) - \gamma_{ig}\left(\frac{1}{2} - \sigma_{ii}^j \right) + \gamma_{xi}\sigma_{xx}^j \right], \\
& \quad \text{(A7)}
\end{aligned}
$$

$$
\begin{aligned}
\dot{\sigma}_{ex}^j = &i\Delta_{eE}^j \sigma_{ex}^j + ig_c^j \sigma_{gx}^j a^\dagger \\
&- i\frac{\chi_{lx}^j}{2} \sigma_{ei}^j e^{-ik_{lx}r_j + i\Delta_{lx}t} \\
&+ \sigma_{ex}^j \left[-\gamma_{eg}\left(\frac{1}{2} - \sigma_{ee}^j \right) + \gamma_{ig}\sigma_{ii}^j - \gamma_{xi}\left(\frac{1}{2} - \sigma_{xx}^j \right) \right]. \\
& \quad \text{(A8)}
\end{aligned}
$$

Here the same notation is used for the 688-nm pump laser as for the 689-nm pump, now with x in place of i. The equations for the four related populations are

$$\dot{\sigma}_{gg}^j = -ig_c^j\big(\sigma_{ge}^j a^\dagger - \sigma_{eg}^j a\big)$$
$$-i\frac{\chi_{li}^j}{2}\big(\sigma_{gi}^j e^{ik_{li}r_j - i\Delta_{li}l t} - \sigma_{ig}^j e^{-ik_{li}r_j + i\Delta_{li}l t}\big)$$
$$+\sigma_{gg}^j\big[\gamma_{eg}\sigma_{ee}^j + \gamma_{ig}\sigma_{ii}^j + \gamma_{xi}\sigma_{xx}^j\big],$$

$$\dot{\sigma}_{ee}^j = ig_c^j\big(\sigma_{ge}^j a^\dagger - \sigma_{eg}^j a\big)$$
$$+\sigma_{ee}^j\big[-\gamma_{eg}\big(1-\sigma_{ee}^j\big) + \gamma_{ig}\sigma_{ii}^j + \gamma_{xi}\sigma_{xx}^j\big],$$

$$\dot{\sigma}_{ii}^j = i\frac{\chi_{li}^j}{2}\big(\sigma_{gi}^j e^{ik_{li}r_j - i\Delta_{li}l t} - \sigma_{ig}^j e^{-ik_{li}r_j + i\Delta_{li}l t}\big)$$
$$-i\frac{\chi_{lx}^j}{2}\big(\sigma_{ix}^j e^{ik_{lx}r_j - i\Delta_{lx}x t} - \sigma_{xi}^j e^{-ik_{lx}r_j + i\Delta_{lx}x t}\big)$$
$$+\sigma_{ii}^j\big[\gamma_{eg}\sigma_{ee}^j - \gamma_{ig}\big(1-\sigma_{ii}^j\big) + \gamma_{xi}\sigma_{xx}^j\big],$$

$$\dot{\sigma}_{xx}^j = i\frac{\chi_{lx}^j}{2}\big(\sigma_{ix}^j e^{ik_{lx}r_j - i\Delta_{lx}x t} - \sigma_{xi}^j e^{-ik_{lx}r_j + i\Delta_{lx}x t}\big)$$
$$+\sigma_{xx}^j\big[\gamma_{eg}\sigma_{ee}^j + \gamma_{ig}\sigma_{ii}^j + \gamma_{xi}\big(1-\sigma_{xx}^j\big)\big]. \tag{A9}$$

The decays which determine the probability of quantum jumps into and out of these four states are equivalent to the following rate equations:

$$\dot{\sigma}_{gg}^j = \gamma_{eg}\big(\sigma_{ii}^j + \sigma_{ee}^j + \sigma_{uu}^j\big),$$
$$\dot{\sigma}_{ee}^j = -\gamma_{eg}\sigma_{ee}^j + \frac{\gamma_{xe}}{2}\big(\sigma_{xx}^j + \sigma_{zz}^j\big),$$
$$\dot{\sigma}_{ii}^j = -\gamma_{ig}\sigma_{ii}^j + \frac{\gamma_{xi}}{2}\big(\sigma_{xx}^j + \sigma_{yy}^j\big),$$
$$\dot{\sigma}_{xx}^j = w_{nx}^j \sigma_{nn}^j + w_{px}^j \sigma_{pp}^j + w_{rx}^j \sigma_{rr}^j - \gamma_x \sigma_{xx}^j. \tag{A10}$$

Here γ_x with a single subscript refers to the total decay rate out of $|x\rangle$. The remaining states are treated using rate-equation approximations which are used to implement discrete quantum jumps not only for decays but also for excitations by the pumping lasers. The rate equation pumping rates are denoted by w. As the $^3S_1$ populations decay rapidly, we neglect deexcitations by pumping lasers to these levels and obtain for the remaining two

$$\dot{\sigma}_{yy}^j = w_{qy}^j \sigma_{qq}^j + w_{sy}^j \sigma_{ss}^j - \gamma_y \sigma_{yy}^j,$$
$$\dot{\sigma}_{zz}^j = w_{nz}^j \sigma_{nn}^j + w_{uz}^j \sigma_{uu}^j + w_{rz}^j \sigma_{rr}^j + w_{tz}^j \sigma_{tt}^j - \gamma_z \sigma_{zz}^j. \tag{A11}$$

This approach is also used for the long-lived states $^3P_0$ and $^3P_2$, and the remaining $m_J = 1$ level of $^3P_1$, for which we

obtain

$$\dot{\sigma}_{nn}^j = -w_{nx}^j \sigma_{nn}^j - w_{nz}^j \sigma_{nn}^j + \gamma_{xn}\big(\sigma_{xx}^j + \sigma_{yy}^j + \sigma_{zz}^j\big),$$
$$\dot{\sigma}_{pp}^j = -w_{px}^j \sigma_{pp}^j + \frac{6}{10}\gamma_{xp}\sigma_{xx}^j,$$
$$\dot{\sigma}_{qq}^j = -w_{qy}^j \sigma_{qq}^j + \frac{3}{10}\gamma_{xp}\big(\sigma_{xx}^j + \sigma_{yy}^j\big),$$
$$\dot{\sigma}_{rr}^j = -w_{rx}^j \sigma_{rr}^j - w_{rz}^j \sigma_{rr}^j + \gamma_{xp}\left(\frac{\sigma_{xx}^j}{10} + \frac{4\sigma_{yy}^j}{10} + \frac{\sigma_{zz}^j}{10}\right),$$
$$\dot{\sigma}_{ss}^j = -w_{sy}^j \sigma_{ss}^j + \frac{3}{10}\gamma_{xp}\big(\sigma_{yy}^j + \sigma_{zz}^j\big),$$
$$\dot{\sigma}_{tt}^j = -w_{tz}^j \sigma_{tt}^j + \frac{6}{10}\gamma_{xp}\sigma_{zz}^j,$$
$$\dot{\sigma}_{uu}^j = -w_{uz}^j \sigma_{uu}^j - \gamma_{eg}\sigma_{uu}^j + \frac{\gamma_{xu}}{2}\big(\sigma_{yy}^j + \sigma_{zz}^j\big). \tag{A12}$$

Finally, the filter-cavity annihilation operators f_k, which are used for calculating the spectrum, evolve according to

$$\dot{f}_k = -i\Delta_{fE}^k f_k - iGa, \tag{A13}$$

where $\Delta_{fE}^k = \omega_f^k - \omega_E$ is the detuning of the kth filter cavity with respect to the unshifted atomic transition. G is the interaction rate with the main cavity, which can be arbitrary (resulting in a scaling factor for the spectral intensity) when back-action on the main cavity is neglected.

APPENDIX B: HOT-BEAM MODEL EQUATIONS

For the hot-atom beam, the equations can be derived from Eq. (3), which yields the following set of equations in a reference frame fixed to the driving laser frequency ω_d:

$$\dot{a} = -\left(i\Delta_{cd} + \frac{\kappa}{2}\right)a - i\frac{\eta}{2} - i\sum_{j=1}^N g_c^j \sigma_{ge}^j,$$
$$\dot{\sigma}_{ee}^j = ig_c^j\big(\sigma_{ge}^j a^\dagger - \sigma_{eg}^j a\big) - \gamma_{eg}\sigma_{ee}^j, \quad \dot{\sigma}_{gg}^j = -\dot{\sigma}_{ee}^j,$$
$$\dot{\sigma}_{ge}^j = ig_c^j\big(\sigma_{ee}^j - \sigma_{gg}^j\big)a - \left(\frac{\gamma_{eg}}{2} + i\Delta_{ed}^j\right)\sigma_{ge}^j,$$
$$\dot{f}_k = -i\Delta_{fd}^k f_k - iGa. \tag{B1}$$

The same notation as in the main text and Appendix A has been used, dropping expectation values. The transverse relativistic Doppler shift is accounted for in the lasing transition frequencies of each atom via the detuning

$$\Delta_{ed}^j = \omega_E \sqrt{1 - \big(v_x^j/c\big)^2} - \omega_d. \tag{B2}$$

[1] D. G. Matei, T. Legero, S. Häfner, C. Grebing, R. Weyrich, W. Zhang, L. Sonderhouse, J. M. Robinson, J. Ye, F. Riehle, and U. Sterr, 1.5 μm Lasers with Sub-10 mHz Linewidth, Phys. Rev. Lett. **118**, 263202 (2017).

[2] J. M. Robinson, E. Oelker, W. R. Milner, W. Zhang, T. Legero, D. G. Matei, F. Riehle, U. Sterr, and J. Ye, Crystalline optical

cavity at 4 K with thermal-noise-limited instability and ultralow drift, Optica **6**, 240 (2019).

[3] W. Zhang, J. M. Robinson, L. Sonderhouse, E. Oelker, C. Benko, J. L. Hall, T. Legero, D. G. Matei, F. Riehle, U. Sterr, and J. Ye, Ultrastable Silicon Cavity in a Continuously Operating Closed-Cycle Cryostat at 4 K, Phys. Rev. Lett. **119**, 243601 (2017).

[4] K. Numata, A. Kemery, and J. Camp, Thermal-Noise Limit in the Frequency Stabilization of Lasers with Rigid Cavities, Phys. Rev. Lett. **93**, 250602 (2004).

[5] D. Meiser, J. Ye, D. R. Carlson, and M. J. Holland, Prospects for a Millihertz-Linewidth Laser, Phys. Rev. Lett. **102**, 163601 (2009).

[6] T. Laske, H. Winter, and A. Hemmerich, Pulse Delay Time Statistics in a Superradiant Laser with Calcium Atoms, Phys. Rev. Lett. **123**, 103601 (2019).

[7] M. A. Norcia, M. N. Winchester, J. R. K. Cline, and J. K. Thompson, Superradiance on the millihertz linewidth strontium clock transition, Sci. Adv. **2**, e1601231 (2016).

[8] M. A. Norcia, J. R. K. Cline, J. A. Muniz, J. M. Robinson, R. B. Hutson, A. Goban, G. E. Marti, and J. Ye, Frequency Measurements of Superradiance from the Strontium Clock Transition, Phys. Rev. X **8**, 021036 (2018).

[9] M. A. Norcia and J. K. Thompson, Cold-Strontium Laser in the Superradiant Crossover Regime, Phys. Rev. X **6**, 011025 (2016).

[10] S. A. Schäffer, M. Tang, M. R. Henriksen, A. A. Jørgensen, B. T. R. Christensen, and J. W. Thomsen, Lasing on a narrow transition in a cold thermal strontium ensemble, Phys. Rev. A **101**, 013819 (2020).

[11] M. Tang, S. A. Schäffer, A. A. Jørgensen, M. R. Henriksen, B. T. R. Christensen, J. H. Müller, and J. W. Thomsen, Cavity-immune spectral features in the pulsed superradiant crossover regime, Phys. Rev. Res. **3**, 033258 (2021).

[12] A. Gogyan, G. Kazakov, M. Bober, and M. Zawada, Characterisation and feasibility study for superradiant lasing in ^{40}Ca atoms, Opt. Express **28**, 6881 (2020).

[13] C. Hotter, L. Ostermann, and H. Ritsch, Cavity sub- and super-radiance enhanced Ramsey spectroscopy, arXiv:2201.09731.

[14] J. G. Bohnet, Z. Chen, J. M. Weiner, D. Meiser, M. J. Holland, and J. K. Thompson, A steady-state superradiant laser with less than one intracavity photon, Nature (London) **484**, 78 (2012).

[15] G. A. Kazakov and T. Schumm, Active optical frequency standard using sequential coupling of atomic ensembles, Phys. Rev. A **87**, 013821 (2013).

[16] G. A. Kazakov and T. Schumm, Active optical frequency standards using cold atoms: Perspectives and challenges, in *Proceedings of the Conference in Neuchatel for European Frequency and Time Forum* (2014), pp. 411–414.

[17] Y. Wang and J. Chen, Superradiant laser with ultra-narrow linewidth based on ^{40}Ca, Chin. Phys. Lett. **29**, 073202 (2012).

[18] J. Chen and X. Chen, Optical lattice laser, in *Proceedings of the 2005 IEEE International Frequency Control Symposium and Exposition* (IEEE, Piscataway, NJ, 2005), pp. 608–610.

[19] K. Debnath, Y. Zhang, and K. Mølmer, Lasing in the superradiant crossover regime, Phys. Rev. A **98**, 063837 (2018).

[20] Y. Zhang, C. Shan, and K. Mølmer, Ultranarrow Superradiant Lasing by Dark Atom-Photon Dressed States, Phys. Rev. Lett. **126**, 123602 (2021).

[21] C. Hotter, D. Plankensteiner, L. Ostermann, and H. Ritsch, Superradiant cooling, trapping, and lasing of dipole-interacting clock atoms, Opt. Express **27**, 31193 (2019).

[22] D. Meiser and M. J. Holland, Steady-state superradiance with alkaline-earth-metal atoms, Phys. Rev. A **81**, 033847 (2010).

[23] F. Haake, M. I. Kolobov, C. Fabre, E. Giacobino, and S. Reynaud, Superradiant Laser, Phys. Rev. Lett. **71**, 995 (1993).

[24] S. B. Jäger, M. J. Holland, and G. Morigi, Superradiant optomechanical phases of cold atomic gases in optical resonators, Phys. Rev. A **101**, 023616 (2020).

[25] T. Maier, S. Kraemer, L. Ostermann, and H. Ritsch, A superradiant clock laser on a magic wavelength optical lattice, Opt. Express **22**, 13269 (2014).

[26] P. Domokos and H. Ritsch, Collective Cooling and Self-Organization of Atoms in a Cavity, Phys. Rev. Lett. **89**, 253003 (2002).

[27] H. Liu, S. B. Jäger, X. Yu, S. Touzard, A. Shankar, M. J. Holland, and T. L. Nicholson, Rugged mHz-Linewidth Superradiant Laser Driven by a Hot Atomic Beam, Phys. Rev. Lett. **125**, 253602 (2020).

[28] J. Chen, Active optical clock, Chin. Sci. Bull. **54**, 348 (2009).

[29] S. B. Jäger, H. Liu, J. Cooper, T. L. Nicholson, and M. J. Holland, Superradiant emission of a thermal atomic beam into an optical cavity, Phys. Rev. A **104**, 033711 (2021).

[30] S. B. Jäger, H. Liu, J. Cooper, and M. J. Holland, Collective emission of an atomic beam into an off-resonant cavity mode, Phys. Rev. A **104**, 053705 (2021).

[31] S. B. Jäger, H. Liu, A. Shankar, J. Cooper, and M. J. Holland, Regular and bistable steady-state superradiant phases of an atomic beam traversing an optical cavity, Phys. Rev. A **103**, 013720 (2021).

[32] A. Bychek, C. Hotter, D. Plankensteiner, and H. Ritsch, Superradiant lasing in inhomogeneously broadened ensembles with spatially varying coupling, Open Res. Eur. **1**, 73 (2021).

[33] G. A. Kazakov and T. Schumm, Stability analysis for bad cavity lasers using inhomogeneously broadened spin-1/2 atoms as a gain medium, Phys. Rev. A **95**, 023839 (2017).

[34] C. B. Silva, F. Famà, S. Zhou, S. A. Schäffer, G. A. Kazakov, B. Pasquiou, S. Bennetts, and F. Schreck, Towards a continuous superradiant laser on the strontium $^1S_0$ - $^3P_0$ transition, Bull. Am. Phys. Soc. **66** (2021).

[35] C.-C. Chen, S. Bennetts, R. G. Escudero, B. Pasquiou, and F. Schreck, Continuous Guided Strontium Beam with High Phase-Space Density, Phys. Rev. Appl. **12**, 044014 (2019).

[36] M. Barbiero, M. G. Tarallo, D. Calonico, F. Levi, G. Lamporesi, and G. Ferrari, Sideband-Enhanced Cold Atomic Source for Optical Clocks, Phys. Rev. Appl. **13**, 014013 (2020).

[37] I. Nosske, L. Couturier, F. Hu, C. Tan, C. Qiao, J. Blume, Y. H. Jiang, P. Chen, and M. Weidemüller, Two-dimensional magneto-optical trap as a source for cold strontium atoms, Phys. Rev. A **96**, 053415 (2017)

[38] J. Li, K. Lim, S. Das, T. Zanon-Willette, C.-H. Feng, P. Robert, A. Bertoldi, P. Bouyer, C. C. Kwong, S.-Y. Lan, and D. Wilkowski, Bi-color atomic beam slower and magnetic field compensation for ultracold gases, arXiv:2209.08479.

[39] S. Zhou, F. Famà, C. B. Silva, M. Tang, Z. Zhang, S. A. Schäffer, C.-C. Chen, B. Pasquiou, S. Bennetts, and F. Schreck, Continuous superradiant laser based on a simple hot atomic beam, in *52nd Annual Meeting of the APS Division of Atomic, Molecular and Optical Physics*, Bull. Am. Phys. Soc. **66**, S03.00004 (2021).

[40] S. Bennetts (private communication).